Cubic-quintic condensate solitons in four-wave mixing

Zhenkun Wu, Yiqi Zhang, Chenzhi Yuan, Feng Wen, Huaibin Zheng, and Yanpeng Zhang*
Key Laboratory for Physical Electronics and Devices of the Ministry of Education and Shaanxi Key Lab of Information Photonic Technique, Xi'an Jiaotong University, Xi'an 710049, China

Min Xiao†
Department of Physics, University of Arkansas, Fayetteville, Arkansas 72701, USA and National Laboratory of Solid State Microstructures and Department of Physics, Nanjing University, Nanjing 210093, China

(Received 2 December 2012; published 16 December 2013)

We experimentally investigate the two-dimensional condensate (optical dropletlike) soliton formation and dynamics of the generated signal and probe beams in four-wave mixing (FWM) process with atomic coherence, under competition between the third- and fifth-order nonlinear susceptibilities. With such competing nonlinearities, mutual transformations among dropletlike fundamental, dipole, and azimuthally modulated vortex FWM solitons are observed. The influence of nonlinear competition on the photonic band gap is also investigated. All the results are obtained under low powers.

DOI: 10.1103/PhysRevA.88.063828 PACS number(s): 42.65.Tg, 42.50.Gy, 42.65.Jx, 42.65.Sf

I. INTRODUCTION

As a fascinating phenomenon in nonlinear systems, optical solitons have been investigated intensively and different types of solitons with different forms of nonlinearities have been experimentally demonstrated [1–4]. It is worth noting that the multidimensional spatial solitons are not stable just with the third-order nonlinearity because of the catastrophic self-focusing effect [1,2]. In order to avoid such an undesirable effect, diverse types of combined nonlinearities were proposed [5]. One of the schemes is to consider the focusing third-order and defocusing fifth-order nonlinear effects simultaneously with a relatively high beam intensity, i.e., to employ the competing cubic-quintic (CQ) nonlinearities [6,7]. In Ref. [8], the two-dimensional (2D) solitons and liquid light condensates (light droplet) analogous to fluid droplets, were theoretically studied in an atomic system with giant CQ nonlinearities enhanced by electromagnetically induced transparency (EIT) [9–11]. On the other hand, very interesting analogies with superfluidity in a CQ nonlinear system were also theoretically reported [12]. Nevertheless, no further experimental investigation of such an interesting prediction has been reported so far.

In this paper, we experimentally demonstrate controllable 2D condensate (optical dropletlike) solitons of the FWM signal and probe transmission with CQ competing nonlinearities in a coherently prepared multilevel atomic medium. Under switchable beam configurations and quality of prepared atomic coherence, transformations among dropletlike fundamental, dipole, and azimuthally modulated vortex (AMV) solitons are also reported, which are achieved by controlling the CQ nonlinearities. Also, manipulation of FWM condensate solitons has been demonstrated by modulating the photonic band gap (PBG) of electromagnetically induced grating (EIG) [13,14] created by the CQ competing nonlinearities in the coherent atomic medium. It is worth mentioning that our results are obtained with quite low powers.

II. THEORETICAL MODEL AND ANALYSIS

As shown in Fig. 1(a), a three-level atomic system is formed by sodium energy levels $|0\rangle$ $(3S_{1/2})$, $|1\rangle$ $(3P_{3/2})$, and $|2\rangle$ $(5D_{5/2})$. The pump beams E_1 and E_1' (E_2 and E_2') and the probe beam E_p connect the transition $|0\rangle \leftrightarrow |1\rangle$ ($|1\rangle \leftrightarrow |2\rangle$) with the atomic resonant frequency Ω_1 (Ω_2). The experimental setup is shown in Fig. 1(b), and the laser beam configuration is given in the inset. The angle θ_1 between E_1 (with frequency ω_1, wave vector $\mathbf{k}_1$, and Rabi frequency G_1) and E_1' (ω_1, $\mathbf{k}'_1$, G_1') is 0 when the cross point of the two beams is at the center of the oven, $\theta_1 > 0$ at the left side and $\theta_1 < 0$ at the right side. The three beams come from the same dye laser DL1 (10 Hz repetition rate, 5 ns pulse width, and 0.04 cm^{-1} linewidth) with frequency detuning $\Delta_1 = \Omega_1 - \omega_1$, and their wave vectors are in the x-o-z plane. E_2 (ω_2, $\mathbf{k}_2$, G_2) and E_2' (ω_2, $\mathbf{k}'_2$, G_2') with an angle θ_2 between them, from another dye laser DL2 (with the same characteristics as the DL1) with $\Delta_2 = \Omega_2 - \omega_2$, are aligned as shown in Fig. 1(b) (E_2 propagates collinearly with E_1), and the wave vectors are in the y-o-z plane. In this system, there will be two FWM processes, one of which satisfies the phase-matching condition $\mathbf{k}_{\mathrm{F1}} = \mathbf{k}_p + \mathbf{k}_1 - \mathbf{k}'_1$ ($\mathbf{k}_{\mathrm{F2}} = \mathbf{k}_p + \mathbf{k}_2 - \mathbf{k}'_2$) with the generated signal E_{F1} (E_{F2}) propagating nearly in the opposite direction of E_1' (E_2').

In such experimental configuration, several (pump and probe) laser beams with spatially nonuniform intensities and the generated FWM signals interact in a large spatial region; therefore the produced spatially varying phase modulations can greatly affect the propagations and spatial patterns of the probe and FWM signals, which are relatively weak compared with the pump beams. The propagations of the probe and FWM signals are governed by the following equations [13]:

$$\frac{\partial E_h}{\partial z} - \frac{i}{2k_h}\nabla_\perp^2 E_h = i\frac{k_h}{2}\left[\chi_h^{(1)} + \chi_h^{(3)}|E|^2 + \chi_h^{(5)}|E|^4\right]E_h + \sum_{m=1,2}\eta_h E_m (E_m')^* E_l \qquad (1)$$

*ypzhang@mail.xjtu.edu.cn
†mxiao@uark.edu

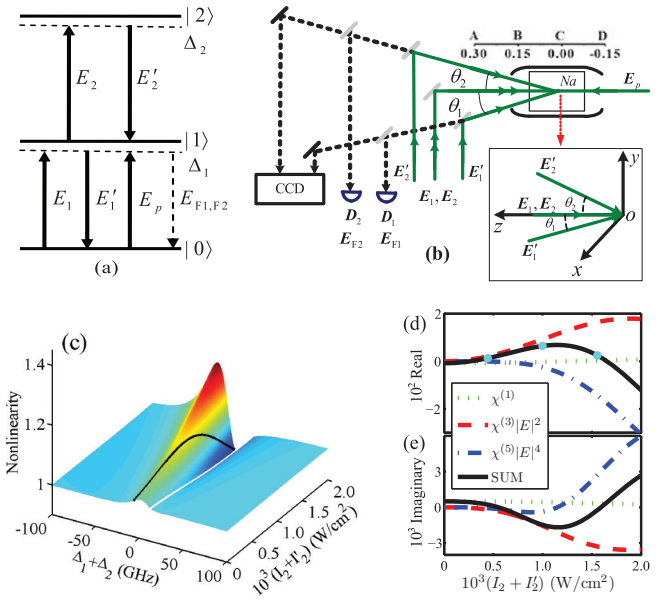

FIG. 1. (Color online) (a) The atomic system. (b) Experimental setup and the optical path diagram. (c) Theoretically NRI versus Δ_2 and $I_2 + I_2'$. The black and white curves are the NRIs at BSP and DSP, respectively. (d) and (e) are, respectively, the theoretical real and imaginary parts of susceptibilities corresponding to the black curve in (c).

with $\chi_h^{(n)}|E|^{n-1} = \chi_h^{(n)S_h}|E_h|^{n-1} + 2\sum_{j=1,2}\chi_h^{(n)X_j}(|E_j|^{n-1} + |E_j'|^{n-1})$. h denotes p or F1 or F2, corresponding to the probe and FWM signals, respectively. The second term on the right-hand side describes the conversion between the probe and FWM signals with η_h being the conversion efficiency. When h is p (F1 or F2), l will take F1 or F2 (p). $\chi_h^{(1)}$, $\chi_h^{(n)S_h}$, and $\chi_h^{(n)X_j}$ ($n = 3$ or 5) represent the linear, the nth-order self-phase modulation (SPM), and cross-phase modulation (XPM) nonlinear susceptibilities, respectively.

In Fig. 1(c), we present the theoretical nonlinear refractive index (NRI) characterizing the XPM of E_2 and E_2' versus $\Delta_1 + \Delta_2$ and $I_2 + I_2'$ with a negative Δ_1. The white line represents the NRI variation at the dark-state point (DSP) at $\Delta_1 + \Delta_2 = 0$ which is uniform; the black curve is at the bright-state point (BSP) that corresponds to the maximum NRI position, which can be adjusted by $I_2 + I_2'$. Corresponding to the black curve in Fig. 1(c) which is taken at a BSP, the dependencies of the real parts of the linear, third-, and fifth-order susceptibilities on $I_2 + I_2'$ are shown in Fig. 1(d) [and Fig. 1(e) for their imaginary parts]. Determined by the real parts of the third- and fifth-order nonlinear susceptibilities, the focusing and defocusing effects follow cubic- and quintic-dependent laws, respectively. The total refractive index composed of the linear part and the XPM nonlinear parts due to E_2 and E_2' can be obtained as $\Delta n = n_1 + \Delta n^{X_2}$, where $\Delta n^{X_2} = \Delta n_2^{X_2} + \Delta n_4^{X_2}$, $\Delta n_2^{X_2} = n_2^{X_2}(I_2 + I_2')$, $\Delta n_4^{X_2} = n_4^{X_2}(I_2^2 + I_2'^2)$, $n_2^{X_2} = \mathrm{Re}[\chi_{p,\mathrm{F1,F2}}^{(3)X_2}]/(\varepsilon_0 c n_1) > 0$, and $n_4^{X_2} = \{4\mathrm{Re}[\chi_{p,\mathrm{F1,F2}}^{(5)X_2}] - \varepsilon_0^2 c^2 (n_2^{X_2})^2\}/(2\varepsilon_0^2 c^2 n_1) < 0$ [8], with $I_2 = \varepsilon_0 c|E_2|^2/2$ ($I_2' = \varepsilon_0 c|E_2'|^2/2$) being the intensity determined by the power P_2 (P_2'). So, when $I_2 + I_2'$ is not large enough, Δn will increase with $I_2 + I_2'$ due to the dominant positive cubic nonlinearity, but as $I_2 + I_2'$ exceeds a threshold, the negative quintic nonlinearity will then play a dominant role on Δn. Thus, the van der Waals–like force from quintic nonlinearity can prevent $E_{p,\mathrm{F1,F2}}$ from collapsing due to the coolinglike mechanism from cubic nonlinearity [8], and assist the formation of stable 2D dropletlike condensate solitons. As shown in Fig. 1(e), the imaginary parts of the susceptibilities that offer gain or loss to the propagations of the probe or FWM signals also experience a competition due to CQ nonlinearities. When $|\mathrm{Im}\{\chi_{p,\mathrm{F1,F2}}^{(1)}\}| \gg |\mathrm{Im}\{\chi_{p,\mathrm{F1,F2}}^{(3)X_2}|E|^2\}| \gg |\mathrm{Im}\{\chi_{p,\mathrm{F1,F2}}^{(5)X_2}|E|^4\}|$ is satisfied, the linear loss is dominant. However, with I_2 (I_2') increasing, the satisfied condition of $|\mathrm{Im}\{\chi_{p,\mathrm{F1,F2}}^{(3)X_2}|E|^2\}| \gg |\mathrm{Im}\{\chi_{p,\mathrm{F1,F2}}^{(1)}\}|$ can make the cubic gain be dominant. If I_2 (I_2') further increases, the quintic loss, i.e., $\mathrm{Im}\{\chi_{p,\mathrm{F1,F2}}^{(5)X_2}|E|^4\}$, will then take charge.

III. EXPERIMENTAL RESULTS AND DISCUSSION

When neglecting diffraction, we can obtain a set of solutions for $E_{p,\mathrm{F1,F2}}$ in Eq. (1) with the nonlinear phase shifts $\phi_{p,\mathrm{F1,F2}} = 2k_{p,\mathrm{F1,F2}} z\Delta n/(n_0 I_{p,\mathrm{F1,F2}})$. The larger this phase shift is, the stronger the nonlinear refraction will be. Also, the spatial modulation on Δn can be transferred to $\phi_{p,\mathrm{F1,F2}}$, and then further to the spatial patterns of $E_{p,\mathrm{F1,F2}}$. Under balanced diffraction and XPM, the probe and FWM signals can form different types of 2D solitons, i.e., fundamental, dipole, and AMV solitons, which can be controlled by adjusting the beam configuration given in Fig. 1(b), as demonstrated later in Figs. 2–4, respectively. More interestingly, transformations among different types of solitons can also be realized by changing CQ nonlinearities, which will be shown in Fig. 3. In the experiment, one can determine the formation of solitons if $E_{p,\mathrm{F1,F2}}$ can maintain their spatial profiles over several diffraction lengths. Such propagation length is easily achieved with the atomic density increased from $1.47 \times 10^{13}/\mathrm{cm}^3$ to $8.37 \times 10^{13}/\mathrm{cm}^3$, i.e., an equivalent propagation distance of

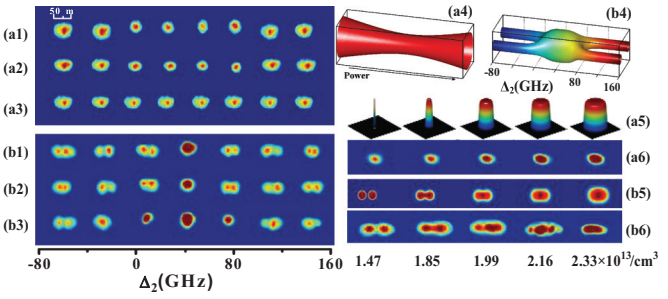

FIG. 2. (Color online) (a) The E_p images versus Δ_2 correspond to the cases of (a1) no beam blocked, (a2) E_2' blocked, and (a3) E_2 and E_2' blocked, respectively. (a4) Isosurface of E_p versus the total pump power. (a5) and (a6) are numerical and experimental formation of a droplet from the middle case in (a2) when the density increases from $1.47 \times 10^{13}/\mathrm{cm}^3$ to $2.33 \times 10^{13}/\mathrm{cm}^3$. (b) The E_{F1} images versus Δ_2 with a decreasing intensity from (b1) to (b3), and (b4) the isosurface of E_{F1} versus Δ_2. (b5) and (b6) are the numerical and experimental coalescence of two droplets from the case right close to the middle in (b2). For all cases, $\Delta_1 = -40$ GHz.

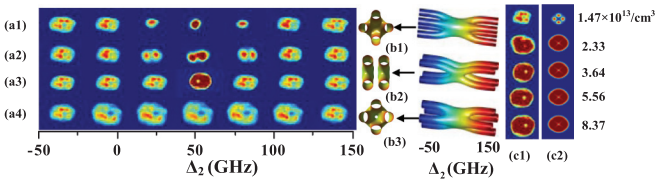

FIG. 3. (Color online) (a) The E_{F1} images versus Δ_2 with $I_2' \approx 10I_2$ and (a1) E_2' blocked, (a2) E_2 blocked, (a3) no beam blocked, (a4) no beam blocked, and $I_2' \approx 20I_2$. (b) The isosurface plots of E_{F1} versus Δ_2 corresponding to (a1)–(a3), respectively. (c) Experimental observation (c1) and numerical simulation (c2) of the formation of a density light dropletlike vortex soliton from the case right close to the middle in (a3).

27 cm, which is almost 17 times longer than the diffraction length of 1.6 cm for a beam with typical diameter of 40 μm.

First, the beam configuration is adjusted to make the E_p transmission have a spatial fundamental mode. The images of the transmitted E_p versus Δ_2 with E_2 and/or E_2' on or off and $\Delta_1 = -43$ GHz are shown in Figs. 2(a1)–2(a3). With E_2' and/or E_2 on, strong focusing of E_p appears when Δ_2 changes from large detuning to the BSP [Figs. 2(a1) and (a2)], while such focusing disappears with E_2 and E_2' both off [Fig. 2(a3)]. This indicates that the XPM of E_2 (E_2') can give rise to a positive Δn, focus E_p beam, and be modulated by the atomic coherence. The comparison between Figs. 2(a1) and 2(a2) can reveal the CQ competition. If only the cubic nonlinearity is considered, $I_2 + I_2'$ in Fig. 2(a1) should bring a stronger focusing at BSP than I_2 alone in Fig. 2(a2), which is contrary to the experimental observation. The reason is that a negative $\Delta n_4^{X_2}$ with large absolute value can effectively weaken the focusing effect due to the positive $\Delta n_2^{X_2}$ in Fig. 2(a1), while in Fig. 2(a2) without E_2, $\Delta n_4^{X_2}$ reduces more than $\Delta n_2^{X_2}$ does, which leads to a relatively larger Δn^{X_2} and strengthens the focusing. The three dots on the solid curve taken at BSP in Fig. 1(d) can elucidate the variation of focusing strength with different $I_2 + I_2'$ values. Figure 2(a4) clearly shows the focusing and defocusing of E_p versus increasing $I_2 + I_2'$,

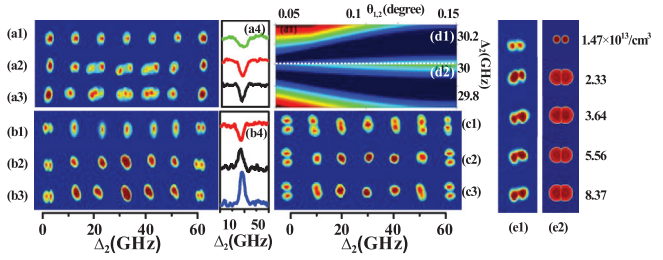

FIG. 4. (Color online) (a) The images of the E_p transmission versus Δ_2 and θ_1 with $\Delta_1 = 30$ GHz [(a1)–(a3)] and the E_p transmission intensities (a4). (b) and (c) are the E_{F1} and E_{F2} images, respectively, and the angle parameters are the same as in (a). (d) Theoretically calculated PBGs (the blue regions) versus Δ_2 and $\theta_{1,2}$ corresponding to $\chi^{(5)}$ (d1) and $\chi^{(3)}$ (d2), respectively. (e) Experimental observation (e1) and numerical simulation (e2) of the formation of density light dropletlike dipole solitons from the extreme right case in (b2).

in which the transverse scaling of the drumlike shape is proportional to the beam width.

Light droplets should have stable flattop localization with a sharp decaying edge. In Figs. 2(a1)–2(a3), under an atomic density $9.1 \times 10^{12}/\text{cm}^3$, even at BSP with significant CQ nonlinearities, a light droplet does not form because of the short propagation length z. With the atomic density rising from $1.47 \times 10^{13}/\text{cm}^3$ to $2.33 \times 10^{13}/\text{cm}^3$ in Fig. 2(a6) and the numerical simulation shown in Fig. 2(a5), the increasing z makes the spot at BSP in Fig. 2(a2) finally evolve into a light droplet, which is named as density light droplet. The mechanism for the formation of a light droplet is the dynamics of E_2 and E_p under CQ nonlinearities. First, E_2 focuses into a sharp peak due to its strong cubic self-Kerr modulation, and then it gets a pit in the peak because of the quintic defocusing effect when the peak surpasses a critical value, and finally a flattop in the spatial profile forms, which mimics a liquid droplet profile. Thus, the XPM leads E_p to form a mediate light droplet, and then a density light droplet.

Next, we investigate the spatial behaviors of FWM signal E_{F1} with E_2' and E_2 both on as shown in Figs. 2(b1)–2(b3). The E_{F1} beam always exhibits a dipole mode with Δ_2 far away from BSP ($\Delta n_2^{X_2}$ is negligible) because of the modulation from the EIG created by E_2 and E_2' [3]. When Δ_2 is at BSP, the dipole mode disappears, but a profile of conspicuous light droplet appears. The reason is that the enhanced $\Delta n_2^{X_2} > 0$ makes the dipole mode collapse into a single spot, and the enhanced $\Delta n_4^{X_2} < 0$ further restrains the excessive collapse, just like the van der Waals–like force. The competition between $\Delta n_2^{X_2}$ and $\Delta n_4^{X_2}$ is clearly shown by the black curve in Fig. 1(c). Different from the light droplet formation in Figs. 2(a5) and 2(a6), those in Figs. 2(b1)–2(b3) form under low density, but with an appropriate detuning, so we can call them detuning light droplets. Because E_p transmission in Fig. 2(a) is not as strong as E_{F1} in Fig. 2(b), detuning light droplets cannot form at BSP, even when $\Delta n_2^{X_2}$ and $\Delta n_4^{X_2}$ are sufficiently large. Comparing the formations of density and detuning light droplets, we can conclude that enhancing $\Delta n_2^{X_2}$ and $\Delta n_4^{X_2}$, and increasing the propagation length z are basically equivalent for the light droplet formation. This can be further verified by the subsequent evolution of dipole mode at Δ_2 deviated from BSP in Fig. 2(b2), which is observed with increasing atomic density as shown in Figs. 2(b5) and 2(b6). We can see that the two dipole humps first form two light droplets, which then fuse into one large mediate light droplet. Comparison among Figs. 2(b1)–2(b3) indicates that different $\Delta n_2^{X_2}$ and $\Delta n_4^{X_2}$ can affect the light droplet profile. Specifically, the detuning light condensate soliton at BSP in Fig. 2(b2) seems to be more compressed than those given in Figs. 2(b1) and 2(b3). In theory, with $I_2 + I_2'$ increasing successively [Figs. 2(b1)–2(b3)], the CQ competition makes Δn first increase and then decrease, which can also be elucidated by the corresponding total susceptibility at BSP (solid curve) in Fig. 1(d), and the three dots (from left to right) on this curve can describe Figs. 2(b1)–2(b3), respectively. On the other hand, as shown in Fig. 1(e) and discussed above, the linear [Fig. 2(b1)] and quintic [Fig. 2(b3)] losses will reduce the beam intensity and slow down the focusing, while the cubic gain [Fig. 2(b2)] will strengthen the focusing. So, the pit in the peak will be

the narrowest one in Fig. 2(b2), and then lead to the smallest flattop.

A more complex spatial mode also can transfer into a light droplet, and the final profile can be controlled by the CQ nonlinearity. In Figs. 3(a1)–3(a4), E_{F1} is modulated into an AMV mode by the interference patterns among E_1, E'_1, and E_p [15] under an appropriate spatial beam configuration, because the XPM from E_2 (E'_2) nearly disappears when Δ_2 is far away from BSP and Δ_1 is set at -53 GHz to provide a weaker focusing background than shown in Fig. 2. The AMV mode can be controlled to form fundamental, dipole or vortex optical droplets, which can all be described by

$$E_\perp(r,\varphi) = (A + Br)\exp(-r^2/R_0)[\cos(C_m\varphi) + i\ \sin(C_m\varphi + B\pi/2)]\exp[i(l\varphi + \phi_{F1})], \quad (2)$$

in which A and B are amplitude coefficients, $2C_m$ is the hump number, l the topological charge, and φ the phase. Specifically, $A = (n_2^{X2}I_2 + n_4^{X2}I_2^2) + |(\Delta_1 + \Delta_2)/\Delta_1|(n_2^{X2}I'_2 + n_4^{X2}I_2'^2)$, $B = (n_2^{X2}I'_2 + n_4^{X2}I_2'^2) + |(\Delta_1 + \Delta_2)/\Delta_1|[n_2^{X1}(I_1 + I'_1) + (n_2^{X2}I_2 + n_4^{X2}I_2^2)]$, and $C_m = m + \exp[-n_2^{X2}(I_2 + I'_2) - n_4^{X2}(I_2^2 + I_2'^2)]$, respectively. In C_m, $m = 0$ for the dipole mode [Fig. 2(b)] and $m = 1$ for the AMV mode (Fig. 3). Around BSP, $|(\Delta_1 + \Delta_2)/\Delta_1| \approx 0$ because the denominator is much larger than the numerator. We can see that $A \approx 0$ at far away from BSP or E_2 is turned off at BSP, and $B \approx 0$ if E'_2 is blocked at BSP. This is consistent with the fact that E_{F1} always shows AMV modes at far away from BSP. With E'_2 blocked and Δ_2 moving towards BSP in Fig. 3(a1), $E_\perp(r,\varphi)$ of E_{F1} changes from AMV to a single-spot structure, and the experimental result shows that a fundamental detuning light droplet forms at BSP. The simulated front and side views of E_{F1} versus Δ_2 in Fig. 3(b1) reveal that the four lobes of AMV fuse into one in the formation of a detuning light droplet. When E_2 is blocked in Fig. 3(a2), $A \approx 0$ but $B \neq 0$ at BSP, C_m has a very small second term because of the large $n_2^{X2}I'_2 + n_4^{X2}I_2'^2$, so $E_\perp(r,\varphi)$ becomes a dipole mode and we experimentally observe a dipole detuning light droplet around BSP. The simulations in Fig. 3(b2) reveal that two pairs of light droplets form from the four lobes in AMV. When no beam is blocked as shown in Fig. 3(a3), balanced total CQ nonlinearities are obtained due to large $I_2 + I'_2$. In this case, $A < B$ because of a stronger E_2 field and $C_m \approx 2$, so $E_\perp(r,\varphi)$ keeps AMV and we experimentally observe a vortex detuning light droplet at BSP. The simulations in Fig. 3(b3) reveal that this AMV evolves into an azimuthally uniform vortex with a phase singularity. In Fig. 3(a4), with I_2 fixed and I'_2 increased, Δn_4^{X2} increases more significantly than Δn_2^{X2}, which breaks the balance between the CQ nonlinearities and makes E_{F1} not form a detuning light droplet due to the lack of initial focusing.

The density light droplet can also form from the AMV mode. Similar to Fig. 2(b5), such evolution has been experimentally observed in Fig. 3(c1) and theoretically simulated in Fig. 3(c2). Here, we increase the medium density from $1.47 \times 10^{13}/\text{cm}^3$ to $8.37 \times 10^{13}/\text{cm}^3$ for the vortex with $\Delta_2 =$ 25 GHz in Fig. 3(a3), during which the four lobes of vortex fuse because a stable droplet needs a circular flattop in which the surface tension is uniform everywhere and helps the pressure of the density light dropletlike vortex soliton reach an equilibrium state [16]. The vortices with appropriate Δ_2 in Figs. 2(a6) and 2(b6) can also form fundamental and dipole density light condensate solitons with sufficiently large density.

The formations of FWM and EIG occur simultaneously, and the latter can affect $E_{p,F1,F2}$ in two aspects. One makes the $E_{F1,F2}$ (E_p) intensity (in transmission) proportional (inversely proportional) to the PBG width, and the other modulates E_{F1} (E_{F2}) into a horizontal (vertical) dipole soliton [3]. The PBG of EIG depends strongly on the nonlinearities. Therefore, the CQ competition can affect the spatial modulations of $E_{p,F1,F2}$ via EIG, which are presented in Fig. 4. Changing θ_1 and/or θ_2 can affect the incident angle of E_p into EIG, which is set at three successively increasing values from Figs. 4(a1) to 4(a3), 4(b1) to 4(b3), and 4(c1) to 4(c3), respectively. For example, by moving the cross point of E_1 and E'_1 from D to B as shown in Fig. 1(b), θ_1 changes from $-0.15°$ to $0.15°$. In Figs. 4(a)–4(c), Δ_1 sets at -33 GHz to have a focusing background stronger than that in Fig. 2. It is obvious that the 2D stable solitons of E_p have no significant variation versus Δ_2 with $\theta_1 = -0.15°$ [Fig. 4(a1)], but when $-0.15° < \theta_1 < 0.15°$ they show a strong spatial splitting near BSP [Figs. 4(a2) and 4(a3), changing θ_2 can generate similar results]. This phenomenon is strongly related to the PBG of the EIG. Specifically, due to the spatial periodic linear, third- and fifth-order susceptibilities, the total refractive index in EIG induced by E_1 and E'_1 is given by $\Delta n_{EIG}(x) = n_1 + \delta n_1\cos(2k_1x) + \delta n_2\cos(4k_1x) + \delta n_4\cos(8k_1x)$, and the PBG width is $\Delta_{gap} = 2\omega_0(\delta n_1 + \delta n_2 + \delta n_4)\sin(\theta_1)/\pi n_1$, where ω_0 is the central frequency; δn_1, δn_2, and δn_4 are the coefficients of different spatial harmonics. Figure 4(d) theoretically shows that the PBG of EIG broadens with increasing $\theta_{1,2}$, so the E_p transmission decreases and gets a larger ϕ_p, which makes E_p easier to modulate into a multispot structure when transmitting through the EIG. In the top curve in Fig. 4(a4), the E_p transmission with $\theta_1 = -0.15°$ shows a suppressed dip around the BSP, because the Bragg reflection (BR) from PBG turns the enhancement into suppression. However, in Fig. 4(a4) with θ_1 increasing, the dip first deepens (the second curve) and then holds almost the same (the bottom curve). That is because the PBG of cubic subgrating broadens faster than that of the quintic one with an increasing θ_1 according to Fig. 4(d). Also, the cubic (quintic) nonlinearity accompanies gain (loss), so the gain will become larger than the loss and compensate the weakened transmission due to PBG. When the effects of PBG, loss and gain reach a balance, the E_p transmission peak will hold.

Figures 4(b) and 4(c) present E_{F1} and E_{F2} images, respectively. Considering their similarities in spatial behavior, we will just discuss E_{F1} in the following text. It is clear to see that the images show a 2D dipole-mode soliton when far away from BSP due to the EIG modulation [3] and focus around BSP. In Figs. 2(b2) and 2(b3), condensate solitons appear around BSP. Since the PBG width increases with the increase of θ_1, more and more energy of E_p will be reflected into E_{F1} that will speed up the formation of condensate solitons. In the intensity curves in Fig. 4(b4), one can find a dip when $\theta_1 = -0.15°$ due to the suppression effect. However, the dip transfers into a peak when θ_1 increases, due to the increased BR of E_p and the switching from suppression to enhancement because of the angle variation. With θ_1 further increased, the

peak gets higher due to the increased BR and the strengthened enhancement.

As done in Figs. 2 and 3, we increase the medium density to study the dipole case in Fig. 4(b2), and have observed the dropletlike dipole solitons ultimately as shown by the experimental and numerical results in Figs. 4(e1) and 4(e2), respectively. It is worth noting that dipole solitons cannot form in Fig. 2(b5) because of the phase relation between the two dipole humps. The dipole mode results from the modulation of EIG so that the lobes are in phase if they locate in the bright or dark stripes simultaneously and out of phase if one of them is in a bright stripe with another in a dark one. The two lobes for the case in Fig. 4(e) are in parallel and almost out of phase (slightly smaller than π), so that dropletlike dipole solitons can form without collision, while the lobes in Fig. 2(b5) can only coalesce because of their in-phase nature [8]. However, the coalescence of the two lobes around BSP in Figs. 4(b2) and 4(b3) seems to be inconsistent with the above explanation. The basic reason is that the lobes of the dipole modes in Fig. 4 are not really exactly out of phase, so the surfaces of the two lobes are not the same as those that are really out of phase, i.e., the nearest neighboring places in the surface will have an energy flow. When the focusing effect is very strong (around the BSP), the energy flow will accelerate and lead to the coalescence as shown in Fig. 4(b). When the focusing is very weak (far away from the BSP), the energy flow will not be strong enough to make the coalescence, such that a dropletlike dipole soliton can form during propagation as shown in Fig. 4(e).

IV. CONCLUSION

In conclusion, we have experimentally investigated the multiparameter controllable FWM condensate solitons under CQ competing nonlinearity enhanced by EIT. A theoretical model has been developed to describe various condensate solitons and transitions among them, which match well with the experimental observations. We would like to emphasize that the experimental results are obtained under low powers. This research can have important applications in spatial pattern formation [17], optical switching [18,19] in optical communication, and all-optical image processing. As far as we know, experimental observations of some interesting theoretical work such as the realization of giant vortices [20], light dripping [21], and new types of quantum phase transitions [22] still remain to be seen.

ACKNOWLEDGMENTS

This work was supported by the 973 program (2012CB921804) and NSFC (Grants No. 61078002, No. 61078020, No. 11104214, No. 61108017, No. 11104216, No. 61205112, and No. 61308015).

[1] M. Mitchell and M. Segev, Nature (London) **387**, 880 (1997).
[2] Z. Chen, M. Mitchell, M. Segev, T. H. Coskun, and D. N. Christodoulides, Science **280**, 889 (1998).
[3] Y. Zhang, Z. Wang, Z. Nie, C. Li, H. Chen, K. Lu, and M. Xiao, Phys. Rev. Lett. **106**, 093904 (2011).
[4] Y. S. Kivshar and G. P. Agrawal, *Optical Solitons: From Fibers to Photonic Crystals* (Academic, San Diego, 2003).
[5] A. H. Piekara, J. S. Moore, and M. S. Feld, Phys. Rev. A **9**, 1403 (1974).
[6] D. E. Edmundson and R. H. Enns, Phys. Rev. A **51**, 2491 (1995).
[7] A. S. Desyatnikov, Y. S. Kivshar, and L. Torner, Prog. Opt. **47**, 291 (2005).
[8] H. Michinel, J. Campo-Táboas, R. García-Fernández, J. R. Salgueiro, and M. L. Quiroga-Teixeiro, Phys. Rev. E **65**, 066604 (2002); H. Michinel, M. J. Paz-Alonso, and V. M. Perez-Garcia, Phys. Rev. Lett. **96**, 023903 (2006).
[9] S. E. Harris, Phys. Today **50**(7), 36 (1997).
[10] M. D. Eisaman, A. André, F. Massou, M. Fleischhauer, A. S. Zibrov, and M. D. Lukin, Nature (London) **438**, 837 (2005).
[11] M. Fleischhauer, A. Imamoglu, and J. P. Marangos, Rev. Mod. Phys. **77**, 633 (2005).
[12] C. Josserand and S. Rica, Phys. Rev. Lett. **78**, 1215 (1997).
[13] Y. Zhang, Z. Nie, and M. Xiao, *Coherent Control of Four-Wave Mixing* (Springer, Heidelberg, 2010).
[14] M. Artoni and G. C. La Rocca, Phys. Rev. Lett. **96**, 073905 (2006).
[15] J. Leach, M. R. Dennis, J. Courtial, and M. J. Padgett, Nature (London) **432**, 165 (2004).
[16] P. G. de Gennes, Rev. Mod. Phys. **57**, 827 (1985).
[17] R. S. Bennink, Vincent Wong, A. M. Marino, D. L. Aronstein, R. W. Boyd, C. R. Stroud, Jr., S. Lukishova, and D. J. Gauthier, Phys. Rev. Lett. **88**, 113901 (2002).
[18] D. N. Christodoulides and E. D. Eugenieva, Phys. Rev. Lett. **87**, 233901 (2001).
[19] A. Chong, W. H. Renninger, D. N. Christodoulides, and F. W. Wise, Nat. Photonics **4**, 103 (2010).
[20] H. Michinel, J. R. Salgueiro, and M. J. Paz-Alonso, Phys. Rev. E **70**, 066605 (2004).
[21] D. Novoa, H. Michinel, and D. Tommasini, Phys. Rev. Lett. **103**, 023903 (2009).
[22] D. Novoa, H. Michinel, D. Tommasini, and M. I. Rodas-Verde, Physica D **238**, 1490 (2009).